Elastic-electro-mechanical modeling and analysis of piezoelectric metamaterial plate with a self-powered synchronized charge extraction circuit for vibration energy harvesting

Zhongsheng Chen[1*], Yemei Xia[1], Jing He[1*], Yeping Xiong[2], Gang Wang[3]

[1] College of Electrical & Information Engineering, Hunan University of Technology, Zhuzhou 417002, P.R. China

[2] Faculty of Engineering and Physical Sciences, University of Southampton, SO16 7QF, UK

[3] State Key Laboratory of Advanced Design and Manufacturing for Vehicle Body, Hunan University, Changsha 410082, P.R. China

Abstract: Structural vibrations usually exist in the form of low-frequency and broadband elastic waves, so cantilever-like harvesters are not appropriate due to space limitations and high quality factor. Piezoelectric metamaterial plate with local resonators (PMP-LR) has been explored to overcome it. However, how to model and analyze the whole energy harvesting system is still a challenge. In this paper, a self-powered synchronized charge extraction circuit is presented and connected to the PMP-LP as the interface circuit. An elastic-electro-mechanical model is built based on the Kirchhoff plate theory and equivalent impedance method, where equivalent impedance of the self-powered synchronized charge extraction circuit is first derived. Then the elastic-electro-mechanical model is numerically solved by using the Bloch theorem and wave finite element method. By numerical simulations, it is found that the synchronized charge extraction circuit has few effects on vibration bandgaps of the PMP-LR. While by inserting an inductor (L_r) parallel with the clamped capacitor (C_p) of the piezoelectric patch, we can see that a new dispersion curve is induced by the $L_r - C_p$ electrical resonance and the inductor is beneficial for low-frequency and broadband vibration energy harvesting. In particular, the inductor can greatly improve the harvesting performance when the resonant frequency is equal to the excitation frequency. In the end, experiments are done and the results are consistent with the numerical ones. Excitingly, the output voltage amplitude of the piezoelectric patch is enlarged about 200% after using the resonant inductor.

Key words: Vibration energy harvesting; piezoelectric metamaterial plate; local resonators; elastic-electro-mechanical model; self-powered synchronized charge extraction circuit with a resonant inductor

Nomenclature

l_a	The length of the base structure	$m(x,y)$	The equivalent mass density
l_b	The width of the base structure	$S(x,y)$	The indicator function
l_c	The side length of the unit cell	$H(*)$	The Heaviside function
l_p	The side length of the piezoelectric patch	$x_{i,1}, y_{i,1}$	The (x, y) coordinates of the left-bottom corner of the i^{th} cell unit
h_s	The thickness of the base structure		
h_p	The thickness of the piezoelectric patch	$x_{i,2}, y_{i,2}$	The (x, y) coordinates of the right-top corner of the i^{th} cell unit
σ_x^s	The stress in the x direction of the base		
ρ_s	The mass densities of the base structure	σ_y^s	The stress in the y direction of the base
ρ_p	The mass densities of the piezoelectric patch	τ_{xy}^s	The stress in the x-y direction of the base
$w(x,y,t)$	Transverse vibration displacement	ε_x^s	The strain in the x direction of the base
σ_x^p	The stress in the x direction of the PZT	ε_y^s	The strain in the y direction of the base

*Corresponding authors. E-mail: chenzs_hut@sina.com, hejing@263.net.

σ_y^p	The stress in the *y* direction of the PZT	γ_{xy}^s	The strain in the *x*-*y* direction of the base
τ_{xy}^p	The stress in the *x*-*y* direction of the PZT	ε_x^p	The strain in the *x* direction of the PZT
$V_p(t)$	The piezoelectric voltage	ε_y^p	The strain in the *y* direction of the PZT
δ	The variational operation	γ_{xy}^p	The strain in the *x*-*y* direction of the PZT
δ_D	The Dirac delta function	m_0	The density of the square mass
E_s	The Young's modulus of the base	μ_p	The Poisson's ratio of the PZT
s_{11}^E	The compliance coefficient at constant electric field intensity	μ_s	The Poisson's ratio of the base
		d_{31}	The 3-1 piezoelectric constant
k	The wave vector	$\bar{\varepsilon}_{33}^S$	The dielectric permittivity at constant strain
D_3	The electric displacement	E_3	The electric field
ω	The angular frequency	θ	The angle between the wave direction and the *x* axis
$\mathbf{\Theta}$	Second-order derivative vector of $w(x,y,t)$	$\boldsymbol{\sigma}_s$	The stress vector of the base
$\boldsymbol{\sigma}_p$	The stress vector of the PZT	$\boldsymbol{\varepsilon}_s$	The strain vector of the base
$\boldsymbol{\varepsilon}_p$	The strain vector of the PZT	$\mathbf{c}_p^E$	The elastic coefficients vector of the PZT
$\mathbf{c}_s^E$	The elastic coefficients vector of the base	$\mathbf{d}_i$	The displacement vector of the i^{th} node
$\mathbf{d}$	The displacement vector of four-node unit	$\boldsymbol{\alpha}$	The vector of polynomial coefficients
$\mathbf{N}$	The shape function matrix	$\mathbf{m}_{uu}$	The mass matrix of four-node unit
$\mathbf{k}_{uu}$	The *x*-stiffness matrix of four-node unit	$\mathbf{k}_{u\phi}$	The coupled stiffness matrix of four-node unit
$\mathbf{k}_{\phi\phi}$	The *y*-stiffness matrix of four-node unit	$\mathbf{M}_{uu}$	The mass matrix of cell unit
$\mathbf{K}_{uu}$	The *x*-stiffness matrix of cell unit	$\mathbf{K}_{\phi\phi}$	The *y*-stiffness matrix of cell unit
$\mathbf{K}_{u\phi}$	The coupled stiffness matrix of cell unit	$\mathbf{u}$	The unit displacement vector
$\mathbf{F}$	The force vector of the cell unit	$\mathbf{I}$	The unit matrix

1. Introduction

As one of promising energy harvesting technologies, piezoelectric vibration energy harvesting can harvest electrical energy from mechanical vibrations based on the direct piezoelectric effect [1-4]. Piezoelectric energy harvesting is superior to other vibration-to-electricity conversion mechanisms due to large energy density and ease of implementation. Thus piezoelectric vibration energy harvesting (PVEH) has been widely studied to realize self-powered WSNs [5]. Most PVEH devices take a form of cantilever, which has some drawbacks from the viewpoints of SHM systems. Firstly, it requires an extra space to hold a bulky proof mass and clamping part. Secondly, it is difficult to effectively harvest low-frequency vibrations due to the length limitation. For SHM, the disadvantages of the cantilever motivated the study of piezoelectric patch-based energy harvesters integrated to the structures to convert vibration energy of their host structure into electrical energy. Piezoelectric patches can be feasible especially for thin structures used in the fields of aerospace, automotive and marine applications. Lee and Youn presented a design and experimental verification methodology for piezoelectric energy harvesting skin, which was optimized by two steps [6]. Later Yoon *et al*

developed an electromechanically-coupled analytical model of PEH skin considering the inertia and stiffness effects of a piezoelectric patch[7]. Erturk presented analytical formulation for energy harvesting with piezoelectric patches from surface fluctuations of large and high impedance structures [8]. Aridogan *et al* [9] derived analytical closed-form expressions of piezoelectric patch-based energy harvesters structurally integrated to fully clamped plates. However, those works mostly focus on a single piezoelectric patch and vibration propagations on the thin plate are often less considered. Structural vibrations are usually variable and exist in the form of elastic waves. Therefore, there is a need to control the propagation of elastic waves, so that vibrations can be concentrated in a local area to be captured effectively. Otherwise, compact and broadband vibration energy harvesting in structures cannot be achieved. The way out of this problem is to develop innovative energy harvesting structures.

In recent years, artificial materials and structures with periodic modulations in their physical properties have attracted significant attention due to their unusual acoustic and elastic properties. Due to material and geometrical discontinuities in the individual cells of periodic structures, waves only propagate along the periodic cells within specific frequency bands. While these waves are completely blocked within other frequency bands called "bandgaps". That is to say, vibration energy within bandgaps can be localized in the cells, which is beneficial for energy harvesting. Thus, we can optimize bandgaps to meet the challenges of low-frequency and broadband PVEH in engineering applications [10]. Periodic structural configurations can help to design both phononic crystals and metamaterials. Gonella *et al* [11] discussed the interplay between phononic bandgaps and piezoelectric microstructures for energy harvesting. Chen *et al* [12] explored one-dimension phononic piezoelectric cantilever beams to widen the resonant bandwidth of a harvester. Chen *et al* first used a phononic crystal to harvest acoustic energy [13]. But for phononic crystal, the lattice constant is required to be on the order of the wavelength, so that its length scale is often large. Liu *et al* [14] firstly proposed the concept of acoustic metamaterial which provided a promising solution for the length-scale problem of band-gap materials. Structural unit sizes of acoustic metamaterials are much smaller than the acoustic wavelength and each unit cell has its own mechanical oscillator. Due to the local resonant behaviors of these auxiliary

oscillators, bandgaps can be created in the low frequency regime. Therefore, locally resonant metamaterials will provide an effective way for harvesting structural vibrations. Sugino *et al* presented analytical and numerical investigations on a one-dimensional locally resonant piezoelectric metastructure with segmented electrodes under transverse vibrations [15]. Hu *et al* studied a mathematical model of an acoustic-elastic metamaterial embedded with a piezoelectric transducer, which was used for simultaneous vibration suppression and energy harvesting [16]. Chen *et al* investigated one kind of 2D piezoelectric metamaterial plates with local resonators (PMP-LR) for structural vibration energy harvesting and pointed out that the location of bandgaps could be designed by adjusting local resonators [17].

For any PVEH system, it is usually composed of two parts. The first part is the harvesting structure which captures vibration energy to electrical energy. The other part is the interface circuit which rectifies and manages the electrical energy for the load. In particular, the harvesting structure and the interface circuit are often coupled due to inverse piezoelectric effect. That is to say, dynamic behaviors of the harvesting structure may be affected by the interface circuit. Conversely, the output voltage of the harvesting structure will affect the performance of the interface circuit. Thus it is much necessary to build its system-level coupling model and perform coupling analysis. Basic function of an interface circuit in PVEH is to realize AC-DC transformation and the simplest interface circuit is a standard full-wave bridge rectifying circuit. However, its transformation efficiency is always low due to the difficulty of impedance matching. To overcome this drawback, switching-based rectifying circuits have been proposed in recent years [18, 19], which can be classified into several groups. The first one is synchronized switching harvesting on an inductor (SSHI) circuits including parallel SSHI (P-SSHI) [20] and series SSHI (S-SSHI) [21], where the switch is placed before the full-wave rectifier. The second one is synchronized charge extraction circuit (SCEC) [22], where the switch is placed after the full-wave rectifier. The third one is called as synchronized switching harvesting on capacitors (SSHC) circuits by using capacitors instead of inductors to flip the voltage. The key of the self-powered circuit is to generate a synchronous switching signal only using ultra-low power consumption. Nowadays, many researchers are studying to make the switching circuit self-powered without external electricity [23, 24].

In the previous work [17], the authors have proposed the PMP-LR for vibration energy harvesting and an analytical model was developed based on the Kirchhoff plate theory. However, no interface circuit is considered. Therefore, this paper will advance the above work to study the PMP-LR with an interface circuit and perform coupling analysis. Compared with P-SSHI and S-SSHI circuits, the most advantage of a SCEC is that its power output is independent of the electric load, eliminating the requirement of impedance matching [25-27]. Equivalent impedances of practical loads vary with excitation frequencies and the PMP-LR is mainly used for broadband vibration energy harvesting, so perfect impedance matching is impossible to be achieved. In this case, a self-powered SCEC is selected as the interface circuit in this paper, also decreasing the difficulty of designing the PMP-LR. The remainder of this paper is organized as follows. In Section 2, an elastic-electro-mechanical model is built based on the Kirchhoff plate theory and equivalent impedance method. At the same time, equivalent impedance of the self-powered SCEC is first derived. Next the elastic-electro-mechanical model is numerically solved by using the Bloch theorem and wave finite element method and in Section 3. In Section 4, numerical simulations are done to analyze effects of the SCEC on the PMP-LR. Experiments are carried out in Section 5 to validate numerical results. Finally, the conclusions of this work are summarized in Section 6.

2. Elastic-electro-mechanical modeling of PMP-LR with a self-powered SCEC

Basic configuration of the PMP-LR with an interface circuit is shown in Fig.1. A thin rectangular plate is used as the base structure and identical square holes are cut off periodically. Then each square hole is covered by a piezoelectric patch that supports a small square mass. The top and bottom electrodes of the piezoelectric patch are connected to the interface circuit. The piezoelectric patch and the mass form a local resonator. Furthermore, each unit cell consists of a base plate-like structure with a square hole, the piezoelectric patch, the small square mass and the interface circuit, which is different from that in [17]. Next we will focus on the elastic-electro-mechanical model of the PMP-LR with the interface circuit.

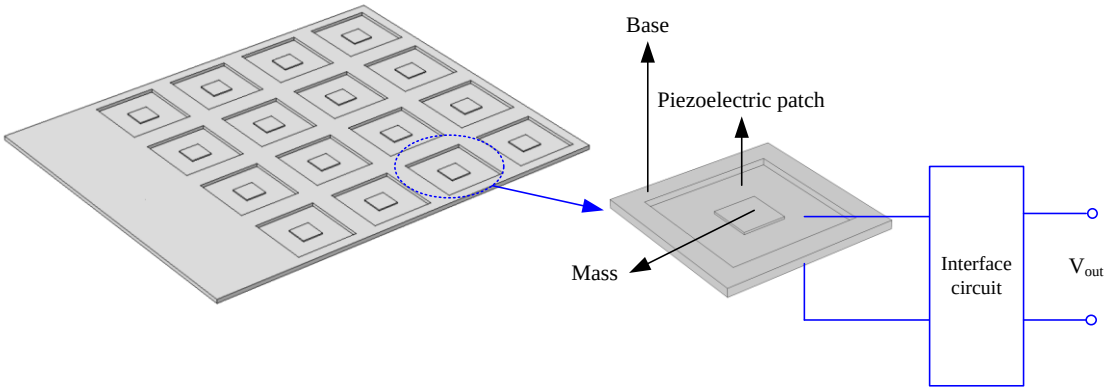

Fig. 1. Basic configuration of a PMP-LR and its interface circuit

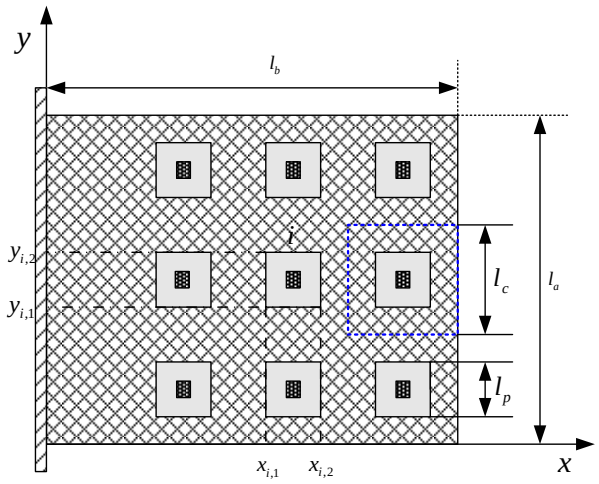

Fig.2. Geometrical dimensions of the PMP-LR

2.1 Dynamic modeling of the PMP-LR

Dynamic modeling of the PMP-LR is outlined here and the details can refer to the work [17].The PMP-LR is assumed to be fixed at the left and its geometrical dimensions are shown in Fig.2. The length and width of the aluminum base structure are denoted as l_b and l_a respectively. The side lengths of the unit cell and the piezoelectric patch are denoted as l_c, l_p, respectively. Thickness of the base structure and the piezoelectric patch are h_s and h_p, respectively. The plane of the PMP-LR corresponds to the x-y plane and the z axis is perpendicular to the x-y plane which is not displayed in Fig.2. A vibration excitation (F_0) perpendicular to the PMP-LR is assumed to act at the location of (x_0, y_0), then transverse vibration displacements will be generated and denote as $w(x, y, t)$. The piezoelectric voltage is denoted as $V_p(t)$. The PMP-LR is modeled as a 2-D Kirchhoff plate, so it will satisfy classical Kirchhoff plate assumptions [7].

Then the Hamilton's principle as Eq.(1) is used to characterize the dynamic equation of the PMP-LR

$$\delta\int_{t_1}^{t_2}\left(KE-PE\right)dt=0 \tag{1}$$

where δ denotes the variational operation, KE and PE are the kinetic and potential energy of the PMP-LR, respectively.

Furthermore, KE is the sum of the kinetic energies of the base structure (KE_s), piezoelectric patches (KE_p) and the mass (KE_m), i.e.,

$$\begin{aligned}KE&=KE_s+KE_p+KE_m\\&=\frac{1}{2}\iint\left[\rho_s h_s+\left(\rho_p h_p-\rho_s h_s\right)S\left(x,y\right)\right]\left(\frac{\partial w\left(x,y,t\right)}{\partial t}\right)^2dxdy\\&+\frac{1}{2}\iint m_0\delta_D\left(x-\frac{x_{i,1}+x_{i,2}}{2}\right)\delta_D\left(y-\frac{y_{i,1}+y_{i,2}}{2}\right)\left(\frac{\partial w\left(x,y,t\right)}{\partial t}\right)^2dxdy\\&\equiv\frac{1}{2}\iint m\left(x,y\right)\dot{w}^2\left(x,y,t\right)dxdy\end{aligned} \tag{2}$$

where $\delta_D\left(*\right)$ is the Dirac delta functions, ρ_s, ρ_p are the mass densities of the base structure and the piezoelectric patch, respectively, $x_{i,1}, y_{i,1}$ are coordinates of the left-bottom corner of the i^{th} cell unit, $x_{i,2}, y_{i,2}$ are coordinates of the right-top corner of the i^{th} cell unit, $m\left(x,y\right)$ denotes the equivalent density of the PMP-LR which is defined as Eq.(3).

$$m\left(x,y\right)=\rho_s h_s+\left(\rho_p h_p-\rho_s h_s\right)S\left(x,y\right)+m_0\delta_D\left(x-\frac{x_{i,1}+x_{i,2}}{2}\right)\delta_D\left(y-\frac{y_{i,1}+y_{i,2}}{2}\right) \tag{3}$$

where, m_0 is the density of the square mass, $S\left(x,y\right)$ is the indicator function of N piezoelectric patches as follows,

$$S\left(x,y\right)=\sum_{i=1}^{N}\left[\left(H\left(x-x_{i,1}\right)-H\left(x-x_{i,2}\right)\right)\right]\left[\left(H\left(y-y_{i,1}\right)-H\left(y-y_{i,2}\right)\right)\right] \tag{4}$$

where $H\left(*\right)$ is the Heaviside unit step function.

Likewise, PE is the sum of potential energies of the base structure (PE_s), piezoelectric patches (PE_p) and the excitation force (PE_F), i.e.,

$$PE=PE_s+PE_p+PE_F \tag{5}$$

Furthermore, we will have,

$$\begin{aligned}PE_s+PE_p&=\frac{1}{2}\iiint\left[\left(1-S\left(x,y\right)\right)\boldsymbol{\sigma}_s^T\boldsymbol{\varepsilon}_s+S\left(x,y\right)\boldsymbol{\sigma}_p^T\boldsymbol{\varepsilon}_p\right]dxdydz\\&=\frac{1}{2}\iiint\left[\left(1-S\left(x,y\right)\right)z^2\boldsymbol{\Theta}^T\mathbf{c}_s^E\boldsymbol{\Theta}w^2\left(x,y,t\right)+S\left(x,y\right)\left(z^2\boldsymbol{\Theta}^T\mathbf{c}_p^E\boldsymbol{\Theta}w^2\left(x,y,t\right)+z\mathbf{e}E_3\boldsymbol{\Theta}^Tw\left(x,y,t\right)\right)\right]dxdydz\\&=\frac{h^3}{24}\iint\left[\boldsymbol{\Theta}^T\left(\left(1-S\left(x,y\right)\right)\mathbf{c}_s^E+S\left(x,y\right)\mathbf{c}_p^E\right)\boldsymbol{\Theta}w^2\left(x,y,t\right)\right]dxdy-\frac{h_p-h_s}{4}\iint S\left(x,y\right)\left(\mathbf{e}V_p\left(t\right)\boldsymbol{\Theta}^Tw\left(x,y,t\right)\right)dxdy\end{aligned} \tag{6}$$

where,

$E_3 = -V_p(t)/h_p$, $\boldsymbol{\Theta} = \left[\partial^2/\partial^2 x \quad \partial^2/\partial^2 y \quad 2\partial^2/\partial x \partial y\right]^T$, $\boldsymbol{\sigma}_s = \left[\sigma_x^s, \sigma_y^s, \tau_{xy}^s\right]^T$, $\boldsymbol{\sigma}_p = \left[\sigma_x^p, \sigma_y^p, \tau_{xy}^p\right]^T$, $\boldsymbol{\varepsilon}_s = \left[\varepsilon_x^s \quad \varepsilon_y^s \quad \gamma_{xy}^s\right]^T$,

$\boldsymbol{\varepsilon}_p = \left[\varepsilon_x^p \quad \varepsilon_y^p \quad \gamma_{xy}^p\right]^T$, $\mathbf{c}_p^E = \dfrac{1}{s_{11}^E(1-\mu_p^2)}\begin{bmatrix} 1 & \mu_p & 0 \\ \mu_p & 1 & 0 \\ 0 & 0 & (1-\mu_p)/2 \end{bmatrix}$, $\mathbf{c}_s^E = \dfrac{E_s}{1-\mu_s^2}\begin{bmatrix} 1 & \mu_s & 0 \\ \mu_s & 1 & 0 \\ 0 & 0 & (1-\mu_s)/2 \end{bmatrix}$, $\mathbf{e} = \dfrac{d_{31}}{s_{11}^E(1-\mu_p)}\begin{bmatrix} 1 \\ 1 \\ 0 \end{bmatrix}$,

d_{31} is the piezoelectric constant in the 3-1 direction, s_{11}^E is the compliance coefficient at constant electric field intensity, $\sigma_x^s, \sigma_y^s, \tau_{xy}^s$ are the stresses in the *x*, *y* and *x-y* directions of the base respectively, $\sigma_x^p, \sigma_y^p, \tau_{xy}^p$ are the stresses in the *x*, *y* and *x-y* directions of the piezoelectric patch respectively, $\varepsilon_x^s \quad \varepsilon_y^s \quad \gamma_{xy}^s$ are the strains in the *x*, *y* and *x-y* directions of the base respectively, $\varepsilon_x^p \quad \varepsilon_y^p \quad \gamma_{xy}^p$ are the strains in the *x*, *y* and *x-y* directions of the piezoelectric patch respectively, μ_s , μ_p are Poisson's ratios of the base structure and the piezoelectric patch respectively, E_s is the Young's modulus of the base, E_3 is the electric field along the *z*-axis.

$$PE_F = -\iint F_0(x_0, y_0, t)\, w(x, y, t)\, dxdy \tag{7}$$

Finally, each term in the left side of Eq.(1) can be calculated as Eq.(8)~Eq.(11).

$$\int_{t_1}^{t_2} \delta KE dt = \int_{t_1}^{t_2} \delta\left[\frac{1}{2}\iint m(x,y)\dot{w}^2(x,y,t)\, dxdy\right] dt = -\int_{t_1}^{t_2}\iint m(x,y)\ddot{w}(x,y,t)\,\delta w dxdydt \tag{8}$$

$$\int_{t_1}^{t_2} \delta\left\{\frac{h_s^3}{24}\iint\left[\boldsymbol{\Theta}^T\left(\left(1-S(x,y)\right)\mathbf{c}_s^E + S(x,y)\mathbf{c}_p^E\right)\boldsymbol{\Theta} w^2(x,y,t)\right] dxdy\right\} dt = \int_{t_1}^{t_2}\iint \boldsymbol{\Theta}^T\mathbf{C}\boldsymbol{\Theta} w(x,y,t)\,\delta w dxdydt \tag{9}$$

where, $\mathbf{C} = \dfrac{h_s^3}{12}\left[\left(1-S(x,y)\right)\mathbf{c}_s^E + S(x,y)\mathbf{c}_p^E\right]$.

$$\int_{t_1}^{t_2} \delta\left[-\frac{h_p - h_s}{4}\iint S(x,y)\left(\mathbf{e}V_p(t)\boldsymbol{\Theta}^T w(x,y,t)\right) dxdy\right] dt = \frac{h_s - h_p}{4}\int_{t_1}^{t_2}\iint S(x,y)\mathbf{e}\boldsymbol{\Theta}^T V_p(t)\,\delta w dxdydt \tag{10}$$

$$\delta\int_{t_1}^{t_2} PE_F dt = -\delta\int_{t_1}^{t_2}\iint F_0(x_0,y_0,t)\, w(x,y,t)\, dxdydt = -\int_{t_1}^{t_2}\iint F_0(x_0,y_0,t)\,\delta w dxdydt \tag{11}$$

Substituting Eq.(8)~Eq.(11) into Eq.(1), we can obtain the dynamic model of the PMP-LR as follows.

$$m(x,y)\frac{\partial^2 w(x,y,t)}{\partial t^2} + \Theta^{\mathrm{T}}\left[\mathbf{C}\left(\Theta w(x,y,t)\right) + \frac{h_s - h_p}{4} S(x,y)\mathbf{e}V_p(t)\right] = F_0(x_0,y_0,t) \tag{12}$$

It can be easily seen that $V_p(t)$ establishes a connection between the harvesting structure and the interface circuit. For the sake of clarity, the abbreviations of all variables will be used in the following work, i.e., $w = w(x,y,t)$,

$V = V_p(t)$, $m = m(x,y)$, $S = S(x,y)$ and $F_0 = F(x_0, y_0, t)$.

2.2 Elastic-electro-mechanical model by using equivalent impedance

According to Fig.1, V is the output voltage of the piezoelectric patch. Each piezoelectric patch in the PMP-LR works under 3-1 mode, so the electric displacement in *z* direction can be reduced to Eq. (13).

$$D_3 = \mathbf{e}^T \boldsymbol{\varepsilon}_p + \bar{\varepsilon}_{33}^S E_3 \tag{13}$$

where, $\bar{\varepsilon}_{33}^S$ is the dielectric permittivity at constant strain, D_3 is the electric displacement along the *z*-axis.

Based on Eqs.(4) and (13), we will have

$$\frac{\partial D_3}{\partial z} = \frac{\partial}{\partial z}\left[\frac{h_s - h_p}{2} S\mathbf{e}^T(\boldsymbol{\Theta} w) - S\bar{\varepsilon}_{33}^S \frac{V}{h_p}\right] = 0 \tag{14}$$

On the other hand, V is the voltage across two terminals of the electric load. Generally speaking, V can be represented as the product of the resistance and the current. While here the electric load is the interface circuit, instead of a pure resistance. Then the voltage V can be written as Eq. (15), where $Z(\omega)$ denotes the impedance of the interface circuit.

$$V(\omega) = j\omega Z(\omega) Q(\omega) \tag{15}$$

where Q is the charge generated by the piezoelectric patch.

By combining Eqs. (12), (14) and (15), the elastic-electro-mechanical model can be represented as,

$$\begin{cases} m\dfrac{\partial^2 w}{\partial t^2} + \Theta^{\mathrm{T}}\left[\mathbf{C}(\Theta w) + \dfrac{h_s - h_p}{4} S\mathbf{e}V\right] = F_0 \\ \dfrac{\partial}{\partial z}\left[\dfrac{h_s - h_p}{2} S\mathbf{e}^T(\boldsymbol{\Theta} w) - S\bar{\varepsilon}_{33}^S \dfrac{V}{h_p}\right] = 0 \\ V(\omega) = j\omega Z(\omega) Q(\omega) \end{cases} \tag{16}$$

Then it can be seen that derivation of $Z(\omega)$ is the most important task to build the elastic-electro- mechanical model.

2.3 Equivalent impedance of a self-powered SCEC

By now, equivalent impedances of standard rectifying and P-SSHI circuits have been derived. To our best knowledge,

however, no counterpart is available for a self-powered SCEC in the literature. In order to derive the equivalent impedance of a self-powered SCEC, firstly it needs to analyze its operation procedure. A typical self-powered SCEC is shown as Fig.3, where a switch is connected after a standard full-wave rectifying circuit. Furthermore, here a self-powered electronic switch circuit similar to that in [24] is adopted, which is composed of three parts: an envelope detector formed by C_1 and D_5, a comparator formed by a PNP transistor T_1, and a switch formed by a NPN transistor T_2. The piezoelectric patch is modeled as a current source $i_{eq}(t)$ parallel with its clamped capacitor C_p. Its principles can be summarized as follows. During each work cycle, the switch remains open in most time except for the two instances when the deflection of the piezoelectric patch reaches the maximum. Once the switch turns on, an $L_1 - C_p$ oscillating loop will be formed and generated charges will be transferred from the piezoelectric patch to the inductor. By this way, vibration energy can be harvested efficiently. In this paper, voltage drops of all diodes are not considered.

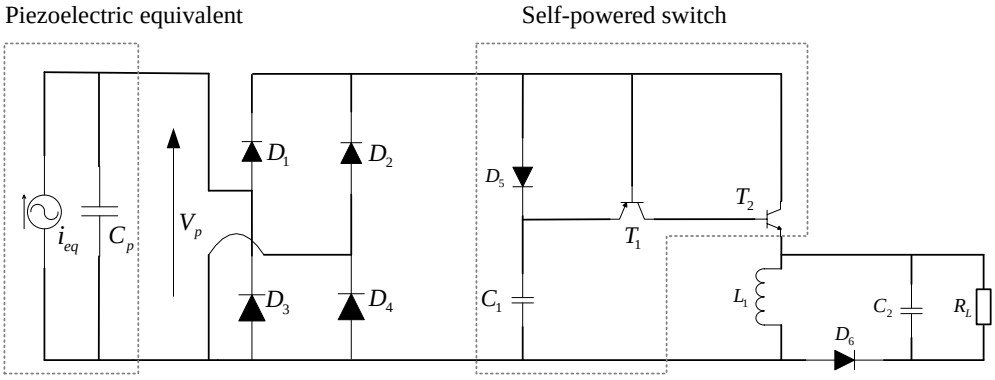

Fig.3. The structure of a self-powered SCEC

In the positive half-period ($0 \sim \pi/\omega$): the two capacitors C_p and C_1 are charged by the current source and the piezoelectric voltage V_p increases until the peak $V_{\max}$. C_p is parallel with C_1, so we will have

$$\frac{C_p}{C_p + C_1} i_{eq}(t) = C_p \frac{dV_p(t)}{dt} \tag{17}$$

When the piezoelectric patch is subjected to a sinusoidal excitation, the current source $i_{eq}(t)$ can be represented as $i_{eq}(t) = I_{eq} \sin(\omega_0 t)$, where I_{eq} is the amplitude and ω_0 is the angular frequency. By performing integration from 0 to

π/ω on both sides of Eq.(17), we will have,

$$\int_0^t \frac{C_p}{C_p + C_1} I_{eq} \sin\left(\omega_0 t'\right) dt' = C_p V_{SCEC}(t) \tag{18}$$

where $V_{SCEC}(t)$ is the input voltage of the SCEC and $V_{SCEC}(t) = V_p(t)$. $V_{SCEC}(t)$ can be obtained from Eq. (18) as follows.

$$V_{SCEC}(t) = \frac{I_{eq}}{\omega_0 \left(C_p + C_1\right)} \left(1 - \cos\left(\omega_0 t\right)\right) \tag{19}$$

Similarly, when the time t varies between π/ω and $2\pi/\omega$, $V_{SCEC}(t)$ can be derived as follows.

$$V_{SCEC}(t) = -\frac{I_{eq}}{\omega_0 \left(C_p + C_1\right)} \left(1 + \cos\left(\omega_0 t\right)\right) \tag{20}$$

Then, $V_{SCEC}(t)$ can be written as a piecewise function as Eq. (21)

$$V_{SCEC}(t) = \begin{cases} \dfrac{I_{eq}}{\omega_0 \left(C_p + C_1\right)} \left(1 - \cos\left(\omega_0 t\right)\right), & 0 \le t \le \dfrac{\pi}{\omega_0} \\ -\dfrac{I_{eq}}{\omega_0 \left(C_p + C_1\right)} \left(1 + \cos\left(\omega_0 t\right)\right), & \dfrac{\pi}{\omega_0} < t \le \dfrac{2\pi}{\omega_0} \end{cases} \tag{21}$$

Next the piecewise function as Eq.(21) can be approximated as Eq. (22) by using the first-order Fourier series expansion.

$$\tilde{V}_{SCEC}(t) = \frac{I_{eq}}{\omega_0 \left(C_p + C_1\right)} \left(\frac{4}{\pi} \sin\left(\omega_0 t\right) - \cos\left(\omega_0 t\right) \right) \tag{22}$$

Fourier transforms of $i_{eq}(t)$ and $\tilde{V}_{SCEC}(t)$ can be calculated as follows.

$$F_{i_{eq}(t)}(\omega) = \frac{I_{eq}}{2j} \left(\delta_D\left(\omega - \omega_0\right) - \delta_D\left(\omega + \omega_0\right) \right) \tag{23}$$

$$F_{\tilde{V}_{SCEC}(t)}(\omega) = \frac{I_{eq}}{\omega\left(C_p + C_1\right)} \left[\frac{2}{j\pi} \left(\delta_D\left(\omega - \omega_0\right) - \delta_D\left(\omega + \omega_0\right) \right) - \frac{1}{2} \left(\delta_D\left(\omega - \omega_0\right) + \delta_D\left(\omega + \omega_0\right) \right) \right] \tag{24}$$

On the other hand, the relationship of equivalent impedances in Fig. 3 can be plotted as Fig.4 and we will have,

$$\frac{1}{Z_{total}} = \frac{1}{Z_{SCEC}} + \frac{1}{Z_{C_p}} \tag{25}$$

where Z_{total}, Z_{SCEC} and Z_{C_p} are equivalent impedances of the total circuit, the SCEC circuit and C_p respectively. Here the

total equivalent impedance can be calculated as,

$$Z_{total}(\omega)=\frac{F_{V_{SCEC}(t)}(\omega)}{F_{i_{eq}(t)}(\omega)} \tag{26}$$

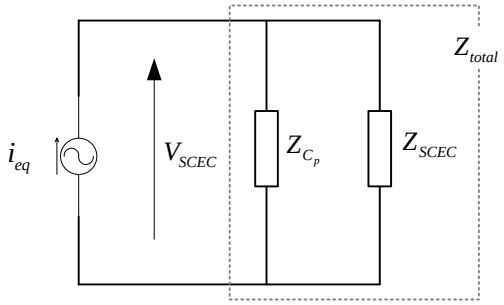

Fig.4. The relationship of three equivalent impedances

By combing Eqs.(23)~(26), we can obtain the equivalent impedance of the self-powered SCEC at $\omega=\omega_0$ as follows.

$$Z_{SCEC}(\omega_0)=\frac{\beta_1\beta_2}{\omega_0\left(1+16/\pi^2\right)\beta_1^2-2\beta_1\beta_2+\beta_2^2}\left[\frac{4}{\pi}\beta_2-j\left(\frac{16}{\pi^2}\beta_1+\beta_1-\beta_2\right)\right] \tag{27}$$

where, $\beta_1=1/\left(C_1+C_p\right)$ and $\beta_2=1/C_p$.

Furthermore, when C_p is much larger than C_1, Eq. (27) can be reduced to Eq.(28).

$$Z_{SCEC}(\omega_0)\approx\frac{\pi}{4\omega_0}\left(\frac{1}{C_p}-j\frac{4}{\pi C_p}\right) \tag{28}$$

3. Numerical solution of the proposed model based on the Bloch theorem and wave finite element method

In order to solve Eq. (16), similar ideas in [28] are referred here. Based on wave propagation characteristics in the PMP-LR, firstly the following field divisions can be carried out based on the Bloch theorem.

$$\begin{bmatrix}w(x,y,t)\\V(x,y,t)\end{bmatrix}=\begin{bmatrix}w_k(x,y)\\V_k(x,y)\end{bmatrix}e^{k\cos\theta x+k\sin\theta y-j\omega t} \tag{29}$$

where, θ is the angle between the wave direction and the *x* axis, k is the wave vector in the first Brillouin zone. For the sake of simplicity, we set

$$\mathbf{H}=\begin{bmatrix}\cos^2\theta\\\sin^2\theta\\2\cos\sin\theta\end{bmatrix},\quad \mathbf{\Gamma}=\begin{bmatrix}\cos\theta & 0\\0 & \sin\theta\\\sin\theta & \cos\theta\end{bmatrix}\begin{bmatrix}\frac{\partial}{\partial x}\\\frac{\partial}{\partial y}\end{bmatrix} \tag{30}$$

Then the first two equations of Eq. (16) can be represented as,

$$-m\omega^2 w_k + \mathbf{\Lambda} w_k + \frac{1}{2} S\mathbf{\Xi} V_k = 0 \tag{31}$$

$$\frac{\partial}{\partial z}\left[S\mathbf{\Xi} w_k - S\bar{\varepsilon}_{33}^s \frac{V_k}{h_p} \right] = 0 \tag{32}$$

where, $\mathbf{\Lambda} = \mathbf{\Theta}^T \mathbf{C}\mathbf{\Theta} + 2k\left(\mathbf{\Theta}^T \mathbf{C}\mathbf{\Gamma} + \mathbf{\Gamma}^T \mathbf{C}\mathbf{\Theta}\right) + k^2\left(\mathbf{\Theta}^T \mathbf{C}\mathbf{H} + \mathbf{H}^T \mathbf{C}\mathbf{\Theta} + 4\mathbf{\Gamma}^T \mathbf{C}\mathbf{\Gamma}\right) + 2k^3\left(\mathbf{\Gamma}^T \mathbf{C}\mathbf{H} + \mathbf{H}^T \mathbf{C}\mathbf{\Gamma}\right) + k^4 \mathbf{H}^T \mathbf{C}\mathbf{H}$ and

$\mathbf{\Xi} = \left(\mathbf{\Theta}^T + 2k\mathbf{\Gamma}^T + k^2 \mathbf{H}^T\right)\left(\frac{h - h_p}{2}\right) S\mathbf{e}$.

Moreover, for any admissible virtual vibration and voltage displacements (δw_k, δV_k), we will have,

$$\int_\Omega \delta w_k \left(-m\omega^2 w_k + \mathbf{\Lambda} w_k + \frac{1}{2} S\mathbf{\Xi} V_k \right) dA = 0 \tag{33}$$

$$\int_\Omega \delta V_k \frac{\partial}{\partial z}\left[S\mathbf{\Xi} w_k - S\bar{\varepsilon}_{33}^s \frac{V_k}{h_p} \right] dA = 0 \tag{34}$$

Based on the divergence theorem, Eqs.(33) and (34) can be calculated as follows.

$$\begin{aligned}
&\int_\Omega \delta w_k \left(-m\omega^2 w_k + \mathbf{\Lambda} w_k + \frac{1}{2} S\mathbf{\Xi} V_k \right) dA \\
&= \int_\Omega -m\omega^2 \delta w_k w_k dA + \int_\Omega \delta\left(\mathbf{\Theta}^T w_k\right)\left(\mathbf{C}\mathbf{\Theta} + 2k\mathbf{C}\mathbf{\Gamma} + k^2 \mathbf{C}\mathbf{H}\right) w_k dA \\
&+ \int_\Omega \delta\left(\mathbf{\Gamma}^T w_k\right)\left(2k\mathbf{C}\mathbf{\Theta} + 4k^2 \mathbf{C}\mathbf{\Gamma} + 2k^3 \mathbf{C}\mathbf{H}\right) w_k dA \\
&+ \int_\Omega \delta w_k \left(k^2 \mathbf{H}\mathbf{C}\mathbf{\Theta} + 2k^3 \mathbf{C}\mathbf{\Gamma} + k^4 \mathrm{H}^{\mathrm{T}} \mathbf{C}\mathbf{H}\right) w_k dA \\
&+ \int_\Omega \delta\left(\mathbf{\Theta}^{\mathrm{T}} w_k\right) \frac{h_s - h_p}{4} S\mathbf{e} V dA + \int_\Omega \delta\left(\mathbf{\Gamma}^{\mathrm{T}} w_k\right) k \frac{h_s - h_p}{2} S\mathbf{e} V dA \\
&+ \int_\Omega \delta w_k k^2 \mathbf{H}^{\mathrm{T}} \frac{h_s - h_p}{4} S\mathbf{e} V dA + \int_s \left(\delta w_k f_k + \delta\theta_{kx} M_x + \delta\theta_{ky} M_y\right) ds
\end{aligned} \tag{35}$$

$$\begin{aligned}
&\int_\Omega \delta V_k \partial\left[S\mathbf{\Xi} w_k - S\bar{\varepsilon}_{33}^s \frac{V_k}{h_p} \right] / \partial z dA \\
&= \int_\Omega \delta E_k \left(\mathbf{\Theta}^T + 2k\mathbf{\Gamma}^T + k^2 \mathbf{H}^T\right)\left(\frac{h_s - h_p}{2}\right) S\mathbf{e} dA - \int_\Omega \delta E_k S\bar{\varepsilon}_{33}^s \frac{V_k}{h_p} dA + \int_\Omega \delta V_k S q_k dA
\end{aligned} \tag{36}$$

Next it needs to derive numerical solution due to the difficulty of analytical method. According to finite element theories, the PMP-LR can be discretized by four-node rectangular units whose length and width are denoted as a, b respectively. Each node has three degrees of freedom (w, θ_x, θ_y) and then generalized displacement of the i^{th} node can be written as,

$$\mathbf{d}_i = \begin{bmatrix} w_i \\ \theta_{xi} \\ \theta_{yi} \end{bmatrix} = \begin{bmatrix} w_i \\ \partial w_i / \partial y \\ -\partial w_i / \partial x \end{bmatrix}, \quad (i = 1, \mathrm{K}\ 4) \tag{37}$$

Displacement vector of each four-node unit can be written as,

$$\mathbf{d} = \begin{bmatrix} \mathbf{d}_1 & \mathrm{L} & \mathbf{d}_4 \end{bmatrix}^T = \begin{bmatrix} w_1 & \theta_{x1} & \theta_{y1} & \mathrm{L} & w_4 & \theta_{x4} & \theta_{y4} \end{bmatrix}^T \tag{38}$$

Furthermore, the displacement w can be approximated as the following polynomial of x, y with twelve unknown coefficients.

$$w(x,y) = \alpha_1 + \alpha_2 x + \alpha_3 y + \alpha_4 x^2 + \alpha_5 xy + \alpha_6 y^2 + \alpha_7 x^3 + \alpha_8 x^2 y + \alpha_9 xy^2 + \alpha_{10} y^3 + \alpha_{11} x^3 y + \alpha_{12} xy^3 \tag{39}$$

Eq.(39) can be rewritten as the following matrix form

$$w = \mathbf{P}\boldsymbol{\alpha} \tag{40}$$

where, $\mathbf{P} = \begin{bmatrix} 1, x, y, x^2, xy, y^2, x^3, x^2 y, xy^2, y^3, x^3 y, xy^3 \end{bmatrix}$, $\boldsymbol{\alpha} = \begin{bmatrix} \alpha_1, \alpha_2, \alpha_3, \alpha_4, \alpha_5, \alpha_6, \alpha_7, \alpha_8, \alpha_9, \alpha_{10}, \alpha_{11}, \alpha_{12} \end{bmatrix}^T$,

Then we will have,

$$\boldsymbol{\theta}_{\mathbf{x}} = \begin{bmatrix} 0, 0, 1, 0, x, 2y, 0, x^2, 2xy, 3y^2, x^3, 3xy^2 \end{bmatrix} \boldsymbol{\alpha} \tag{41a}$$

$$\boldsymbol{\theta}_{\mathrm{y}} = \begin{bmatrix} 0, -1, 0, 0, -2x, -y, 0, -3x^2, -2xy, -y^2, 0, -3xy^2, -y^3 \end{bmatrix} \boldsymbol{\alpha} \tag{41b}$$

Eq.(40) can be rewritten as,

$$w = \mathbf{N}\mathbf{d} \tag{42}$$

where $\mathbf{N}=\mathbf{P}\mathbf{A}^{-1}$ is the shape function matrix and,

$$\mathbf{A} = \begin{bmatrix}
1 & -a & -b & a^2 & ab & b^2 & -a^3 & -a^2 b & -ab^2 & -b^3 & a^3 b & ab^3 \\
0 & 0 & 1 & 0 & -a & -2b & 0 & a^2 & 2ab & 3b^2 & -a^3 & -3ab^2 \\
0 & -1 & 0 & 2a & b & 0 & -3a^2 & -2ab & -b^2 & 0 & 3a^2 b & b^3 \\
1 & a & -b & a^2 & -ab & b^2 & a^3 & -a^2 b & ab^2 & -b^3 & -a^3 b & -ab^3 \\
0 & 0 & 1 & 0 & a & -2b & 0 & a^2 & -2ab & 3b^2 & a^3 & 3ab^2 \\
0 & -1 & 0 & -2a & b & 0 & -3a^2 & 2ab & -b^2 & 0 & 3a^2 b & b^3 \\
1 & a & b & a^2 & ab & b^2 & a^3 & a^2 b & ab^2 & b^3 & a^3 b & ab^3 \\
0 & 0 & 1 & 0 & a & 2b & 0 & a^2 & 2ab & 3b^2 & a^3 & 3ab^2 \\
0 & -1 & 0 & -2a & -b & 0 & -3a^2 & -2ab & -b^2 & 0 & -3a^2 b & -b^3 \\
1 & -a & b & a^2 & -ab & b^2 & -a^3 & a^2 b & -ab^2 & b^3 & -a^3 b & -ab^3 \\
0 & 0 & 1 & 0 & -a & 2b & 0 & a^2 & -2ab & 3b^2 & -a^3 & -3ab^2 \\
0 & -1 & 0 & 2a & -b & 0 & -3a^2 & 2ab & -b^2 & 0 & -3a^2 b & -b^3
\end{bmatrix} \tag{43}$$

By using the shape function, we will have

$$\boldsymbol{\Theta} w = \begin{bmatrix} \dfrac{\partial^2}{\partial^2 x} & \dfrac{\partial^2}{\partial^2 y} & \dfrac{2\partial^2}{\partial x \partial y} \end{bmatrix}^T \mathbf{N}\mathbf{d} = \mathbf{B}\mathbf{d} \tag{44a}$$

$$\boldsymbol{\Gamma} w = \begin{bmatrix} \cos\theta & 0 \\ 0 & \sin\theta \\ \dfrac{\sin\theta}{2} & \dfrac{\cos\theta}{2} \end{bmatrix} \begin{bmatrix} \dfrac{\partial}{\partial x} \\ \dfrac{\partial}{\partial y} \end{bmatrix} \mathbf{N}\mathbf{d} = \mathbf{L}\mathbf{d} \tag{44b}$$

where, $\mathbf{B}=\begin{bmatrix} \dfrac{\partial^2}{\partial^2 x} & \dfrac{\partial^2}{\partial^2 y} & \dfrac{2\partial^2}{\partial x \partial y} \end{bmatrix}^T \mathbf{N}$, $\mathbf{L} = \begin{bmatrix} \cos\theta & 0 \\ 0 & \sin\theta \\ \dfrac{\sin\theta}{2} & \dfrac{\cos\theta}{2} \end{bmatrix} \begin{bmatrix} \dfrac{\partial}{\partial x} \\ \dfrac{\partial}{\partial y} \end{bmatrix} \mathbf{N}$.

Based on Eqs.(42)~(44), the mass, stiffness and coupled stiffness matrixes of each four-node unit can be calculated as,

$$\begin{aligned} \mathbf{m}_{uu} &= \int_\Omega \mathbf{N}^T m(x,y) \mathbf{N} dxdy \\ &= \int_\Omega \mathbf{N}^T \left[\rho_s h_s + \left(\rho_p h_p - \rho_s h_s\right) S(x,y) + m_0 \delta_D \left(x - \frac{x_{i,1}+x_{i,2}}{2} \right) \delta_D \left(y - \frac{y_{i,1}+y_{i,2}}{2} \right) \right] \mathbf{N} dxdy \end{aligned} \tag{45}$$

$$\begin{aligned} \mathbf{k}_{uu} = &\int_\Omega \mathbf{B}^T \mathbf{C} \mathbf{B} dxdy + 2k \int_\Omega \left(\mathbf{B}^T \mathbf{C} \mathbf{L} - \mathbf{L}^T \mathbf{C} \mathbf{B} \right) dxdy + k^2 \int_\Omega \left(\mathbf{B}^T \mathbf{C} \mathbf{H} + \mathbf{H}^T \mathbf{C} \mathbf{B} - 4\mathbf{L}^T \mathbf{C} \mathbf{L} \right) dxdy \\ &+ 2k^3 \int_\Omega \left(\mathbf{H}^T \mathbf{C} \mathbf{L} - \mathbf{L}^T \mathbf{C} \mathbf{H} \right) dxdy + k^4 \int_\Omega \mathbf{H}^T \mathbf{C} \mathbf{H} dxdy \end{aligned} \tag{46}$$

$$\mathbf{k}_{u\phi} = \int_\Omega \mathbf{B}^T \frac{h_s - h_p}{2} \mathbf{S}\mathbf{e} dxdy - 2k \int_\Omega \mathbf{L}^T \frac{h_s - h_p}{2} \mathbf{S}\mathbf{e} dxdy + k^2 \int_\Omega \mathbf{H}^T \frac{h_s - h_p}{2} \mathbf{S}\mathbf{e} dxdy \tag{47}$$

$$\mathbf{k}_{\phi\phi} = -\int_\Omega S \frac{\bar{\varepsilon}_{33}^s}{h_p} dxdy \tag{48}$$

By assembling all four-node units, we can obtain the mass matrix($\mathbf{M}_{uu}$), stiffness matrix($\mathbf{K}_{uu}$, $\mathbf{K}_{\phi\phi}$) and coupled stiffness matrix ($\mathbf{K}_{u\phi}$) of the cell unit.

$$\mathbf{M}_{uu} \ddot{\mathbf{u}} + \mathbf{K}_{uu} \mathbf{u} + \frac{1}{2} \mathbf{K}_{u\phi} V_k = \mathbf{F} \tag{49}$$

$$\mathbf{K}_{u\phi} \mathbf{u} + \mathbf{K}_{\phi\phi} V_k = Q \tag{50}$$

where $\mathbf{F}$ is the force vector. By denoting $Y(\omega) = 1/\left(j\omega Z(\omega) \right)$, Eq.(50) can be rewritten as Eq.(51) based on Eq.(15).

$$\mathbf{K}_{u\phi} \mathbf{u} + \left(\mathbf{K}_{\phi\phi} - Y(\omega) \right) V_k = 0 \tag{51}$$

Then Eqs.(49) and (51) can be represented as the following matrix form.

$$\begin{bmatrix} -\omega^2 \mathbf{M}_{uu} + \mathbf{K}_{uu} & \dfrac{1}{2} \mathbf{K}_{u\phi} \\ \mathbf{K}_{u\phi}^T & \mathbf{K}_{\phi\phi} - Y(\omega) \end{bmatrix} \begin{bmatrix} \mathbf{u} \\ V_k \end{bmatrix} = \begin{bmatrix} \mathbf{F} \\ 0 \end{bmatrix} \tag{52}$$

Furthermore, Eq.(52) can be arranged as a polynomial form of wave vector k.

$$\mathbf{D}(\omega,k,\theta)=\begin{bmatrix}-\omega^2\mathbf{M}_{uu}+\mathbf{K}_{uu}^0 & \frac{1}{2}\mathbf{K}_{u\phi}^0\\ \left(\mathbf{K}_{u\phi}^1\right)^T & \mathbf{K}_{\phi\phi}-Y(\omega)\end{bmatrix}+k\begin{bmatrix}\mathbf{K}_{uu}^1 & \frac{1}{2}\mathbf{K}_{u\phi}^1\\ \left(\mathbf{K}_{u\phi}^1\right)^T & 0\end{bmatrix}$$
$$+k^2\begin{bmatrix}\mathbf{K}_{uu}^2 & \frac{1}{2}\mathbf{K}_{u\phi}^2\\ \left(\mathbf{K}_{u\phi}^2\right)^T & 0\end{bmatrix}+k^3\begin{bmatrix}\mathbf{K}_{uu}^3 & 0\\ 0 & 0\end{bmatrix}+k^4\begin{bmatrix}\mathbf{K}_{uu}^4 & 0\\ 0 & 0\end{bmatrix} \tag{53}$$

where $\mathbf{K}_{uu}^0$, $\mathbf{K}_{uu}^1$, $\mathbf{K}_{uu}^2$, $\mathbf{K}_{uu}^3$ and $\mathbf{K}_{uu}^4$ are the absolute, monomial, quadratic, cubic and quartic terms of k in $\mathbf{K}_{uu}$, $\mathbf{K}_{u\phi}^0$、$\mathbf{K}_{u\phi}^1$ 和 $\mathbf{K}_{u\phi}^2$ are the absolute, monomial and quadratic terms of k in $\mathbf{K}_{u\phi}$.

Based on the Bloch theorem, periodic boundary conditions of the unit cell can be written as,

$$\begin{bmatrix}\mathbf{u}\\ V_k\end{bmatrix}=\mathbf{T}\begin{bmatrix}\hat{\mathbf{u}}\\ V_k\end{bmatrix} \tag{54a}$$

$$\mathbf{T}^T\begin{bmatrix}\mathbf{F}\\ 0\end{bmatrix}=0 \tag{54b}$$

where, $\hat{\mathbf{u}}=\begin{bmatrix}\mathbf{u}_{\mathrm{I}} & \mathbf{u}_{\mathrm{B}} & \mathbf{u}_{\mathrm{L}} & \mathbf{u}_{\mathrm{LB}}\end{bmatrix}$, $\mathbf{T}=\begin{bmatrix}\mathbf{I} & 0 & 0 & 0 & 0 & 0 & 0 & 0 & 0 & 0\\ 0 & \mathbf{I} & \mathbf{I} & 0 & 0 & 0 & 0 & 0 & 0 & 0\\ 0 & 0 & 0 & \mathbf{I} & \mathbf{I} & 0 & 0 & 0 & 0 & 0\\ 0 & 0 & 0 & 0 & 0 & \mathbf{I} & \mathbf{I} & \mathbf{I} & \mathbf{I} & 0\\ 0 & 0 & 0 & 0 & 0 & 0 & 0 & 0 & 0 & 1\end{bmatrix}^T$ and $\mathbf{I}$ is the unit matrix.

Substituting Eq.(54) into Eq.(52), we will have,

$$\mathbf{T}^T\mathbf{D}(\omega,k,\theta)\mathbf{T}\begin{bmatrix}\hat{\mathbf{u}}\\ V_k\end{bmatrix}=0 \tag{55}$$

The non-zero solution condition of Eq.(55) is that the determinant of $\mathbf{T}^T\mathbf{D}(\omega,k,\theta)\mathbf{T}$ is equal to zero. In this case, we will have,

$$(\mathbf{D}_0+k\mathbf{D}_1+k^2\mathbf{D}_2+k^3\mathbf{D}_3+k^4\mathbf{D}_4)\mathbf{X}=0 \tag{56}$$

where, $\mathbf{X}=\begin{bmatrix}\hat{\mathbf{u}} & V_k\end{bmatrix}^T$, $\mathbf{D}_0=\mathbf{T}^T\begin{bmatrix}-\omega^2\mathbf{M}_{uu}+\mathbf{K}_{uu}^0 & \frac{1}{2}\mathbf{K}_{u\phi}^0\\ \left(\mathbf{K}_{u\phi}^1\right)^T & \mathbf{K}_{\phi\phi}-Y(\omega)\end{bmatrix}\mathbf{T}$, $\mathbf{D}_1=\mathbf{T}^T\begin{bmatrix}\mathbf{K}_{uu}^1 & \frac{1}{2}\mathbf{K}_{u\phi}^1\\ \left(\mathbf{K}_{u\phi}^1\right)^T & 0\end{bmatrix}\mathbf{T}$,

$\mathbf{D}_2=\mathbf{T}^T\begin{bmatrix}\mathbf{K}_{uu}^2 & \frac{1}{2}\mathbf{K}_{u\phi}^2\\ \left(\mathbf{K}_{u\phi}^2\right)^T & 0\end{bmatrix}\mathbf{T}$, $\mathbf{D}_3=\mathbf{T}^T\begin{bmatrix}\mathbf{K}_{uu}^3 & 0\\ 0 & 0\end{bmatrix}\mathbf{T}$, $\mathbf{D}_4=\mathbf{T}^T\begin{bmatrix}\mathbf{K}_{uu}^4 & 0\\ 0 & 0\end{bmatrix}\mathbf{T}$.

Then Eq.(56) can be transformed to a standard eigenvalue equation as Eq.(57).

$$\left(\mathbf{G}-k\mathbf{I}\right)\hat{\mathbf{X}}=0 \tag{57}$$

where, $\mathbf{G}=\begin{bmatrix} 0 & \mathbf{I} & 0 & 0 \\ 0 & 0 & \mathbf{I} & 0 \\ 0 & 0 & 0 & \mathbf{I} \\ -\mathbf{D}_4^{-1}\mathbf{D}_0 & -\mathbf{D}_4^{-1}\mathbf{D}_1 & -\mathbf{D}_4^{-1}\mathbf{D}_2 & -\mathbf{D}_4^{-1}\mathbf{D}_3 \end{bmatrix}$, $\hat{\mathbf{X}}=\begin{bmatrix} \mathbf{X} \\ k\mathbf{X} \\ k^2\mathbf{X} \\ k^3\mathbf{X} \end{bmatrix}$.

By solving Eq.(57), we can obtain k, $\mathbf{X}$ and $\hat{\mathbf{u}}$. Furthermore, we can calculate $\mathbf{u}$, V_k by combing Eq.(54a) with Eq.(49). Next, we can obtain $\mathbf{d}$ from $\mathbf{u}$, which can be used to calculate w based on Eq.(42). Therefore, numerical solution of the elastic-electro-mechanical model is achieved.

4. Simulations on coupling analysis

In order to verify the above theoretical results, numerical simulations are done in this section. Firstly, geometric and material parameters of the PMP-LR are listed in Table 1 and Table 2. Effects of geometric parameters have been studied in the previous paper [17], so this paper mainly focuses on key electric parameters.

Table 1. Geometric parameters of the PMP-LR in simulations

	PZT patch	PZT base	Mass	Plate
Length	90mm	90mm	30mm	100mm
Width	90mm	90mm	30mm	100mm
Height	0.2mm	0.5mm	15mm	3mm

Table 2. Material parameters of the PMP-LR in simulations

	Material	Young's modulus(Gpa)	Possion's ratio	Density(kg/m^3)
PZT base	Al	70	0.33	2700
PZT patch	PZT-5H	31	0.29	7500
Mass	Steel	200	0.30	7870

4.1 Feasibility of the equivalent impedance of the self-powered SCEC

According to basic principle of the self-powered SCEC, its harvested energy can be looked as the accumulated energy in C_p. The excitation source is assumed as $i_{eq}(t)=I_{eq}\sin(\omega_0 t)$, then the harvested energy in half cycle can be calculated as,

$$W=\frac{1}{2}C_p V_{SCEC}^2\left(\pi/\omega_0\right) \tag{58}$$

By using the approximation value of $V_{SCEC}(t)$ in Eq.(22), we will have

$$\%V_{SCEC}(\pi/\omega_0)=\frac{2I_{eq}}{(C_p+C_1)\omega_0} \tag{59}$$

Thus theoretic value of the harvested power in half cycle is calculated as,

$$P_h^t=\frac{2I_{eq}^2C_p}{\pi\omega_0(C_p+C_1)^2} \tag{61}$$

On the other hand, the self-powered SCEC is simulated in the Multisim12.0 software. Firstly, the circuit in Fig.3 is built and the piezoelectric patch is replaced by i_{eq} and C_p. In each simulation, different groups of component parameters listed in Table 3 are selected. Then the simulated voltage $V_{SCEC}(t)$ is measured and its peak value can be obtained. Furthermore, the harvested power in half cycle (P_h^s) is calculated by Eq.(58). At the same time, $\%V_{SCEC}(t)$ and P_h^t can be calculated by Eq.(22) and Eq.(61). Finally, simulated and approximated $V_{SCEC}(t)$ are compared in Fig.5 and P_h^t and P_h^s are compared in Table 3 ($\Delta P=\left|\left(P_h^t-P_h^s\right)/P_h^s\right|\times 100\%$).

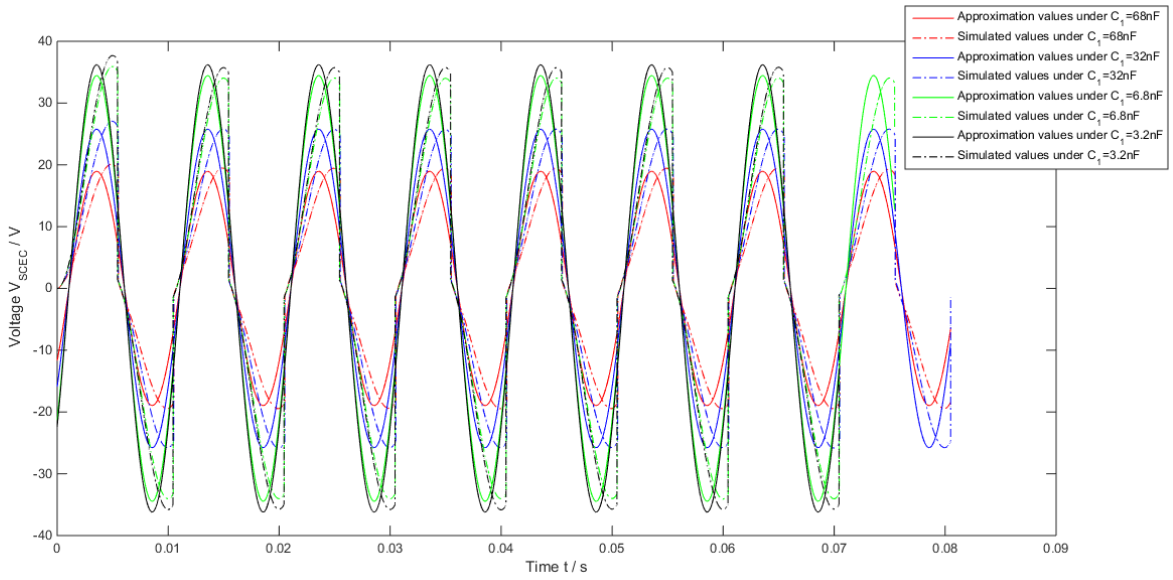

Fig.5. Comparisons of simulated and approximated $V_{SCEC}(t)$ under $\omega_0=200\pi$

Table 3. Comparisons of P_h^t and P_h^s

I_{eq}	ω_0	C_p	C_1	C_r	L_1	R_L	P_h^t	P_h^s	ΔP
0.001A	200π	68nF	68nF	20 μF	2nH	100 KΩ	3.7mW	3.6mW	2.78
0.001A	200π	68nF	32nF	20 μF	2nH	100 KΩ	6.8mW	6.9mW	1.45
0.001A	200π	68nF	6.8nF	20 μF	2nH	100 KΩ	12.3mW	12.1mW	1.65
0.001A	200π	68nF	3.2nF	20 μF	2nH	100 KΩ	13.6mW	13.5mW	0.74

From Fig.5 and Table 3, we can see that: i) $\%V_{SCEC}(t)$ is close to the simulated results and ΔP is very small (less than 3%); ii) The reasons of derivations may include neglecting both voltage drops of all diodes and the time delay of the electronic switch in theoretical calculations [24], the series expansion approximation bias in Eq. (22), simulation bias, estimation bias of C_P, etc;. Therefore, the equivalent impedance of the self-powered SCEC is feasible.

4.2 Effects of the self-powered SCEC with a resonant inductor on vibration bandgaps

In the numerical simulations, it is found that the self-powered SCEC has few effects on vibration bandgaps of the PMP-LR. In order to explain this phenomenon, we relook at the working process of the self-powered SCEC. The self-powered switch remains open in most time. In this case, we can find that electronic load of each unit cell is just composed of $D_1 \sim D_5$ and C_1. Furthermore, the equivalent impedance of the self-powered SCEC as Eq.(28) is almost independent of C_1 when C_p is much larger than C_1. Next, vibration bandgaps before and after inserting C_1 are simulated and shown in Fig.6. It can be seen that vibration bandgaps hardly change. Based on these simulated and theoretical results, it is feasible to understand that the coupled influence of the SCEC is very small.

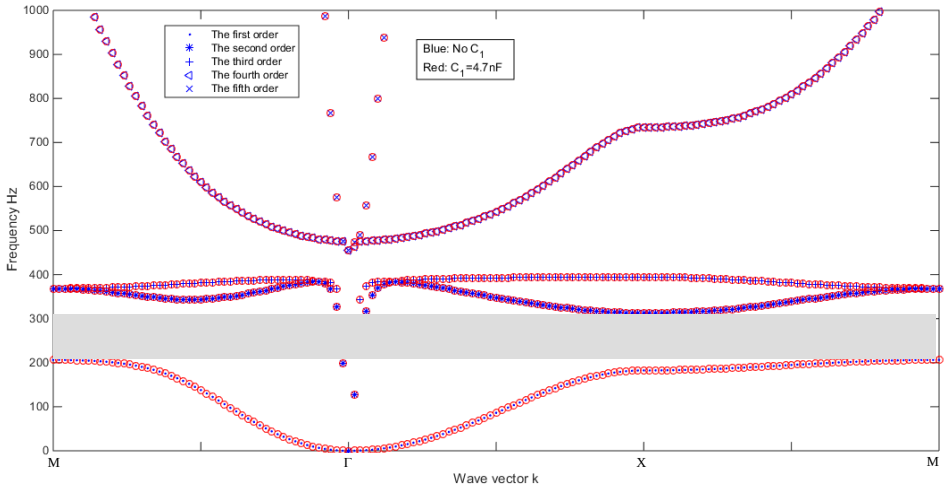

Fig.6. Comparison of dispersion curves before and after inserting C_1

Surprisingly, however, we find that an inductor load has obvious effects on vibration responses of the PMP-LR by simulations. Therefore, we insert an inductor L_r parallel with C_p in Fig.3. For example, we set $L_r = 1\text{H}$ here. Dispersion curves before/after inserting the inductor are calculated by using the numerical solution and then shown in Fig. 7 respectively. We can see from Fig.7 that a new dispersion curve is generated due to inserting the inductor L_r and its mean value is about 190Hz. In order to explain it, we calculate the $L_r - C_p$ resonant frequency as follows.

$$f_{re} = \frac{1}{2\pi\sqrt{L_r C_p}} = 197.4\text{Hz} \tag{62}$$

Obviously, f_{re} is very close to the frequency corresponding to the new dispersion curve. Therefore, we can conclude that the new dispersion curve is induced by the $L_r - C_p$ electrical resonance. Similar phenomenon has been reported in

[29]. At the same time, there is a little difference between the two frequencies and the reasons may include simulation bias, estimation bias of C_P, etc. In addition, it can be found from Fig.7 that the first-order dispersion curve shifts to low-frequency regions, while the second-order, third-order and fourth-order ones shifts to high-frequency regions. Excitingly, the results demonstrate that inserting an inductor can enlarge the first-order bandgap and benefit for low-frequency and broadband PVEH.

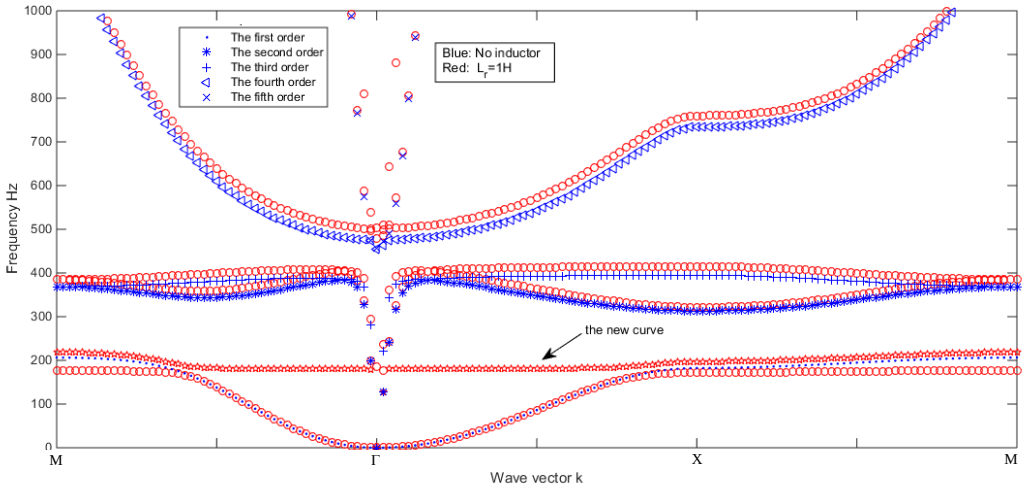

Fig.7. Comparison of dispersion curves before and after inserting an inductor

4.3 Effects of L_r on output voltage of the piezoelectric patch

Besides of the above advantage of L_r, we also strongly focus on its effects on output voltage of the unit cell. Firstly, an excitation force is applied on the free end of the PMP-LR and the amplitude and frequency are 10N, 197Hz respectively. Each simulation time is 0.1s and the convergence time is at about 0.04s. During the simulation, different values of L_r and excitation frequencies are used and then output voltages of the unit cell are calculated respectively. Firstly, the results in three cases of $L_r = 0.1\text{H}$, $L_r = 1\text{H}$, $L_r = 10\text{H}$ are plotted in Fig.8. According to the simulation results, we can find that the amplitude of output voltage will reach the maximum only when $L_r = 1\text{H}$. Based on Eq.(62), we can see that the $L_r - C_p$ resonant frequency approximates the excitation frequency when $L_r = 1\text{H}$.

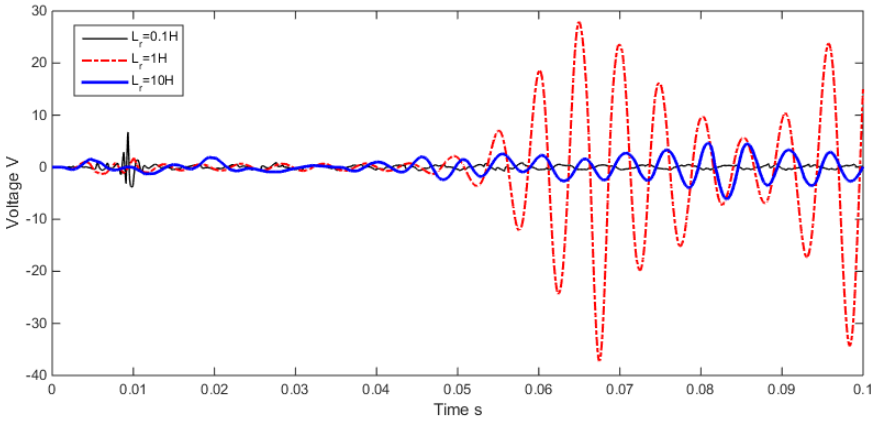

Fig.8. Output voltages of the piezoelectric patch using different inductors

Secondly, the results in three cases of 100Hz, 197Hz, 300Hz with $L_r = 1\mathrm{H}$ are plotted in Fig.9 and the similar conclusion can be achieved. Therefore, we can believe the value of L_r also has strong effects on harvesting performance of the PMP-LR. In practice, we should choose L_r so that the $L_r - C_p$ resonant frequency is equal to the excitation frequency. In the case of broadband excitations, the $L_r - C_p$ resonant frequency may be selected to be the central frequency of the bandgap.

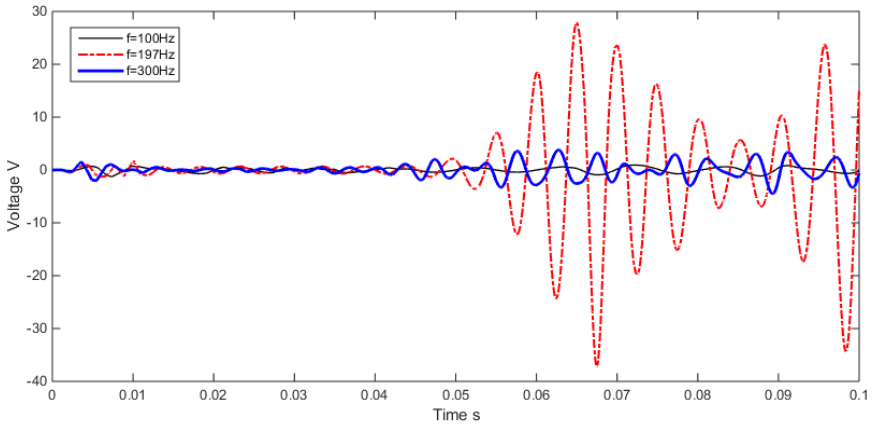

Fig.9. Output voltages of the piezoelectric patch using different excitation frequencies

4.4 Frequency response of a finite-period PMP-LR

In order to testify the first-order bandgap, a finite-period PMP-LP with 10×10 cell units is built by finite element modeling. The excitation is located at the center of the PMP-LR and the response is located at the boundary of the PMP-LR. The excitation frequency is swept from 0Hz to 500Hz. Then frequency responses are calculated and shown in Fig.10. We can see that vibrations falling among 224Hz~305Hz are prohibited, which just approximates the first-order bandgap.

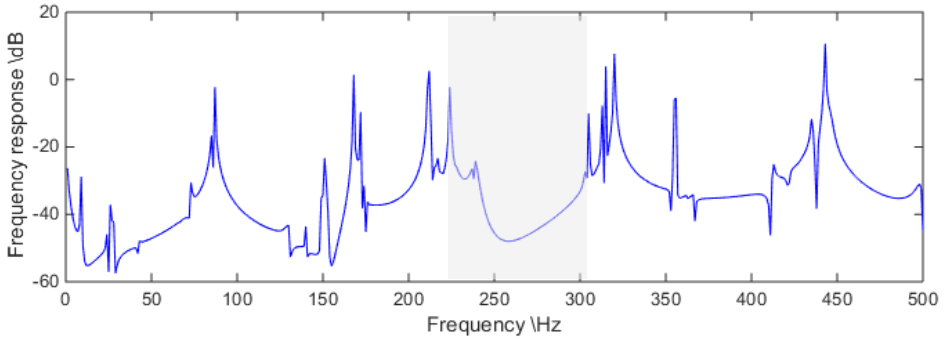

Fig.10. Frequency response of the PMP-LR with 10×10 cell units

5. Experimental tests

An experimental set-up is built as shown in Fig.11, which is composed of a PMP-LR, a power amplifier, a vibration shaker, a Polytec vibration scanner and an oscilloscope. Then a PMP-LR composed of 4×4 unit cells is fabricated and

its geometric and material parameters are listed in Table 1 and Table 2. The PCB of the self-powered SCEC is designed and made for experimental testing.

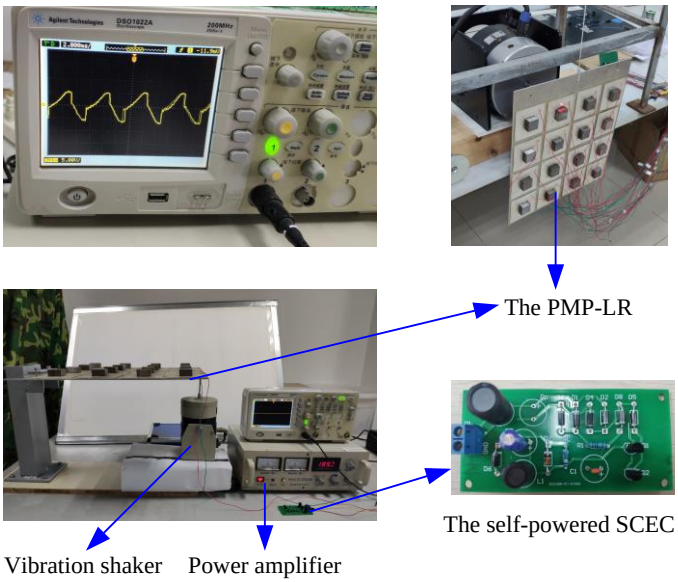

Fig.11. Experimental set-up

In the experiments, the component parameters of the self-powered SCEC is chosen as C_1=4.7nF , L_r=1H , L_1=0.22mH , C_2=47μF and R_L=10Ω according to optimized results. A harmonic excitation force with the frequency of 189.3Hz (close to the optimal value of numerical results) is generated by the shaker and the excitation location is at the center of the free end of the PMP-LR. Then output voltages of both piezoelectric patches and the SCEC are recorded and analyzed.

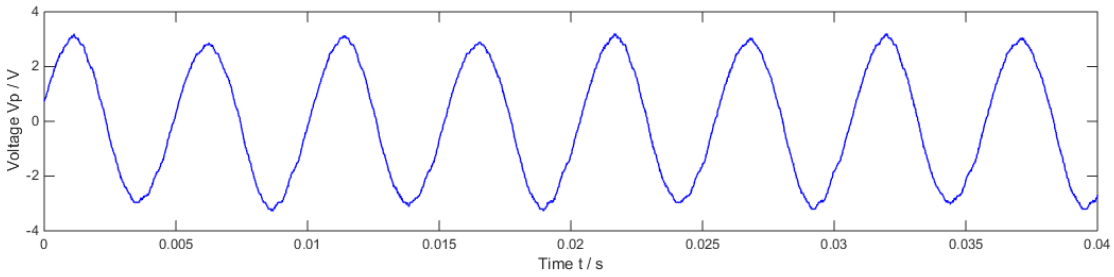

Fig.12. Open-circuit voltage of the piezoelectric patch

Firstly, the self-powered SCEC is not connected and the open-circuit voltage waveform of the piezoelectric patch is shown in Fig.12. We can see that the open-circuit voltage is also harmonic with the same frequency as the excitation frequency.

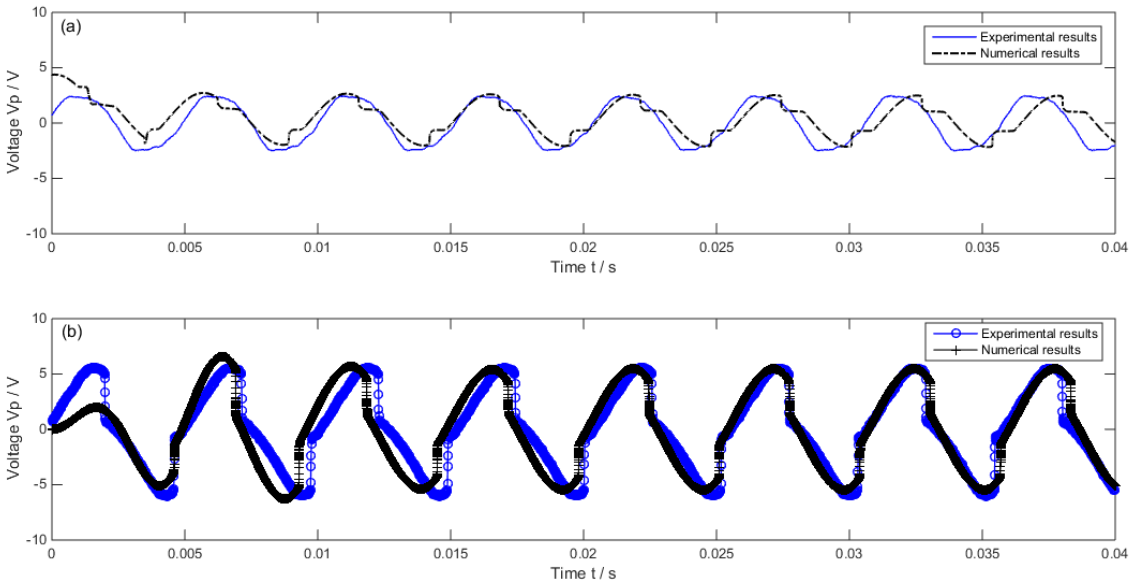

Fig.13. Output voltages of the piezoelectric patch (a) without and (b) with L_r

Next, the self-powered SCEC without and with L_r are connected respectively and the corresponding output voltages of the piezoelectric patch are recorded and plotted in Fig.13. In the case of no L_r, we can see that the self-powered SCEC doesn't work well due to low piezoelectric voltage. In this case, the intrinsic drawback of the full-bridge rectifying circuit is prominent and the voltage amplitude is clamped due to the conduction of rectifying diodes. Thus harvested energy from the piezoelectric patch is low. While L_r is used, we can see that the voltage inversion phenomenon is obvious and the voltage amplitude is enlarged about 200%. Therefore it is validated that inserting an inductor can greatly improve the harvesting performance of the PMP-LR, which is consistent to the numerical results.

6. Conclusions

In this paper, a self-powered SCEC as the interface circuit is connected to the PMP-LP for harvesting structural vibration energy. Elastic-electro-mechanical model of the whole PVEH system is built and solved numerically. Finally, numerical simulations and experiments were done to validate the model. Main highlights of this paper may include: i) An elastic-electro-mechanical model is built based on the Kirchhoff plate theory and equivalent impedance method. Equivalent impedance of the self-powered SCEC is first derived; ii) The elastic-electro-mechanical model is numerically solved by using the Bloch theorem and wave finite element method; iii) It is discovered that the SCEC has

few effects on vibration bandgaps of the PMP-LR in most time. While inserting an inductor parallel with the clamped capacitor of the piezoelectric patch can generate a new dispersion curve, enlarge the first-order bandgap and decrease the frequency band region, which is much beneficial for low-frequency and broadband PVEH; iv) Inserting the inductor can greatly improve the harvesting performance once the inductor-capacitor resonant frequency is equal to the excitation frequency. In the future, it needs to study how to select the optimal inductor for given broadband vibrations and topology optimization methods can be further used to optimize the whole system [30].

Acknowledgement

This work was supported by the National Natural Science Foundations of China (Grant Nos. 51577189, 51911530202 and 11772123). Also the first and fourth authors will thank the support by the Royal Society under the International Exchanges Scheme-Cost Share Programme (Grant No. IEC\NSFC\181462).

References

[1]J. L. Wang, S. X. Zhou, Z. E Zhang, D. Yurchenko, High-performance piezoelectric wind energy harvester with Y-shaped attachments, Energ. Convers. Manage. 181(2)(2019) 645-652.

[2]J. L. Wang, L. H.Tang, L. Y. Zhao, Z. E. Zhang, Efficiency investigation on energy harvesting from airflows in HVAC system based on galloping of isosceles triangle sectioned bluff bodies, Energy, 172(2019) 1066-1078.

[3]S. X. Zhou, J. L. Wang, Dual serial vortex-induced energy harvesting system for enhanced energy harvesting, AIP Advances, 8(7)(2018) 075221.

[4]Z. H. Lai, J. L. Wang, C. L. Zhang, G. Q. Zhang, D. Yurchenko, Harvest wind energy from a vibro-impact DEG embedded into a bluff body, Energ. Convers. Manage. 199(2019) 111993.

[5] P. Cahill, B. Hazra, R. Karoumi, A. Mathewson, V. Pakrashi, Vibration energy harvesting based monitoring of an operational bridge undergoing forced vibration and train passage, Mech. Syst. Signal Pr. 106(2018) 265-283.

[6] S. Lee, B. D. Youn, A design and experimental verification methodology for an energy harvester skin structure, Smart Mater. Struct. 20 (2011) 057001.

[7] H. Yoon, B. D. Youn, H. S. Kim, Kirchhoff plate theory-based electromechanically-coupled analytical model considering inertia and stiffness effects of a surface-bonded piezoelectric patch, Smart Mater. Struct. 25(2016) 025017.

[8] A. Erturk, Piezoelectric energy harvesting for civil infrastructure system applications: moving loads and surface strain fluctuations, J. Intel. Mat. Syst. Str. 22 (2011) 1959-1973.

[9] U. Aridogan, I. Basdogan, A. Erturk, Analytical modeling and experimental validation of a structurally integrated piezoelectric energy harvester on a thin plate, Smart Mater. Struct. 23 (2014) 045039.

[10] Z. S. Chen, B. Guo, Y. M. Yang, C. C. Cheng, Metamaterials-based enhanced energy harvesting: A review, Physica B 438 (2014) 1-8.

[11]S. Gonella, A. To, W. K. Liu, Interplay between phononic bandgaps and piezoelectric microstructures for energy harvesting, J. Mech. Phys. Solids 57(3)(2009) 621-633.

[12]Z. S. Chen, Y. M. Yang, Z. M. Lu, Y. T. Luo, Broadband characteristics of vibration energy harvesting using one-dimensional phononic piezoelectric cantilever beams, Physica B 410(2013) 5-12.

[13]L. Y. Wu, L. W. Chen, C. M. Liu, Acoustic energy harvesting using resonant cavity of a sonic crystal, Appl. Phys. Lett. 95 (2009) 013506.

[14]Z. Y. Liu, X. X. Zhang, Y. W. Mao, Y. Y. Zhu, Z. Y. Yang, C. T. Chan, P. Sheng, Locally resonant sonic materials, Science, 289 (2000) 1734-1736.

[15]C. Sugino, S. Leadenham, M. Ruzzene, A. Erturk, An investigation of electroelastic bandgap formation in locally resonant piezoelectric metastructures, Smart Mater. Struct. 26 (2017) 055029.

[16]G. B. Hu, L.H. Tang, A. Banerjee, R. Das, Metastructure with piezoelectric element for simultaneous vibration suppression and energy harvesting, J. Vib. Acoust. 139 (2017) 011012.

[17]Z. S. Chen, J. He, G. Wang, Vibration bandgaps of piezoelectric metamaterial plate with local resonators for vibration energy harvesting, Shock Vib. 2019(2019) 1397123.

[18]D. Guyomar, A. Badel, E. Lefeuvre, C. Richard, Toward energy harvesting using active materials and conversion

improvement by nonlinear processing, IEEE T. Ultrason. Ferr. 52(4)(2005) 584-595.

[19]W. Q. Liu, A. Badel, F. Formosa, Q. Zhu, C. Zhao, G. D. Hu, A comprehensive analysis and modeling of the self-powered synchronous switching harvesting circuit with electronic breakers. IEEE T. Ind. Electron. 65(5)(2018) 3899-3909.

[20]S. Lu, F. Boussaid, A highly efficient P-SSHI rectifier for piezoelectric energy harvesting, IEEE T. Ind. Electron. 30(10) (2015) 5364-5369.

[21]I. C. Lien, Y. C. Shu, W. J. Wu, S. M. Shiu, H.C. Lin, Revisit of series-SSHI with comparisons to other interfacing circuits in piezoelectric energy harvesting, Smart Mater. Struct. 19(12)(2010) 125-134.

[22]E. Lefeuvre, A. Badel, C. Richard, D. Guyomar, Piezoelectric energy harvesting device optimization by synchronous electric charge extraction, J. Intel. Mat. Syst. Str. 16(10)(2005) 865-876.

[23] J.R. Liang, W.H. Liao, Improved design and analysis of self-powered synchronized switch interface circuit for piezoelectric energy harvesting systems, IEEE T. Ind. Electron. 59(4)(2012) 1301-1312.

[24] Z. S. Chen, J. He, J. L. Liu, Y. P. Xiong, Switching delay in self-powered nonlinear piezoelectric vibration energy harvesting circuit: mechanisms, effects, and solutions, IEEE T. Power Electr. 34(3)(2019) 2427-2440.

[25] L.Y. Zhao, L.H. Tang, Y. W. Yang. Synchronized charge extraction in galloping piezoelectric energy harvesting, J. Intel. Mat. Syst. Str. 27(4)(2015) 453-468.

[26] L. H. Tang, Y. W. Yang. Analysis of synchronized charge extraction for piezoelectric energy harvesting, Smart Mater. Struct. 20(8)(2011) 085022.

[27] J. L. Wang, L. H. Tang, L.Y. Zhao, G. B. Hu, R. J. Song, X. Kun. Equivalent circuit representation of a vortex-induced vibration-based energy harvester using a semi-empirical lumped parameter approach. Int. J Energ. Res. (2020) doi: 10.1002/ER.5228.

[28] S. B. Chen, J. H. Wen, G. Wang, X. S, Wen, Tunable band gaps in acoustic metamaterials with periodic arrays of resonant shunted piezos, Chin. Phys. B 22(7)(2013) 074301.

[29] N. Kherraz, L. Haumesser, F. Levassort, P. Benard, B. Morvan, Hybridization bandgap induced by an electrical resonance in piezoelectric metamaterial plates, J. Appl. Phys. 123(2018) 094901.

[30] J.Q. Wang, Simultaneous vibration suppression and energy harvesting: Damping optimization for performance limit, Mech. Syst. Signal Pr. 132(2019) 609-621.